Ore Geology Reviews 49 (2012) 96–108

Contents lists available at SciVerse ScienceDirect

Ore Geology Reviews

journal homepage: www.elsevier.com/locate/oregeorev

Fractional crystallization and the formation of thick Fe–Ti–V oxide layers in the Baima layered intrusion, SW China

Xiao-Qi Zhang [a,b], Xie-Yan Song [a,*], Lie-Meng Chen [a], Wei Xie [a], Song-Yue Yu [a], Wen-Qin Zheng [a], Yu-Feng Deng [a], Jia-Fei Zhang [c], Shu-Guang Gui [c]

[a] State Key Laboratory of Ore Deposit Geochemistry, Institute of Geochemistry, Chinese Academy of Sciences, Guiyang 550002, China
[b] Graduate University of the Chinese Academy of Sciences, Beijing 100049, China
[c] Mining Company of Panzhihua Group Company Limited, Sichuan 617000, China

ARTICLE INFO

Article history:
Received 5 February 2012
Received in revised form 4 September 2012
Accepted 6 September 2012
Available online 14 September 2012

Keywords:
Emeishan Large Igneous Province
Baima layered intrusion
Fe–Ti oxide
Closed to oxygen system
Magma replenishment
MELTS

ABSTRACT

The Baima layered intrusion is located in the central part of the Emeishan Large Igneous Province (ELIP). The N–S striking intrusion is ~24 km long and ~2 km thick and dips to the west. Based on variations in modal proportions and cumulus mineral assemblages, the intrusion from the base to the top is simply subdivided into a lower zone (LZ) with most of the economic magnetite layers, and an upper zone (UZ) with apatite-bearing troctolite and gabbro. The rock textures suggest crystallization of the Fe–Ti oxide slightly later than plagioclase (An_{67-54}) but relatively earlier than olivine (Fo_{74-55}), followed by clinopyroxene and finally apatite.

Relatively low olivine forsterite content and abundant ilmenite exsolution lamellae in clinopyroxene indicate that the Baima parental magma is a highly evolved Fe–Ti-rich magma. Via MELTS model, it demonstrates that under a closed oxygen system, extensive silicate mineral fractionation of a picritic magma might lead to Fe and Ti enrichment and oxygen fugacity elevation in the residual magma. When such Fe–Ti-rich magma ascends to the shallower Baima intrusion, the Fe–Ti oxides may become an early liquidus phase. Well-matched olivine and plagioclase microprobe data with the results of MELTS calculation, combined with relatively low CaO content in olivine (0.02–0.08 wt.%) indicate that wall-rock contamination probably plays a weak role on oxygen fugacity elevation and the early crystallization of Fe–Ti oxides. Several reversals in whole-rock chromium and plagioclase anorthite contents illustrate that multiple recharges of such Fe–Ti-rich magma mainly occurred along the lower part of the Baima magma chamber. Frequent Fe–Ti-rich magma replenishment and gravitational sorting and settling are crucial for the development of thick Fe–Ti oxide layers at the base of the Baima layered intrusion.

1. Introduction

The study of layered intrusions has provided valuable insights into the processes of igneous differentiation, crystallization and the formation of magmatic ore deposits (Cawthorn, 1996; Wager and Brown, 1968 and references therein). Geochemistry and petrogenesis studies in the past few years have improved our understanding on the origin of the mafic–ultramafic layered intrusions and their hosting Fe–Ti oxide ores in the Emeishan Large Igneous Province (ELIP), SW China. For example, recent zircon U–Pb dating indicated that these layered intrusions were formed in the Late Permian (~260 Ma) and were related to the Emeishan mantle plume (Zhong and Zhu, 2006; Zhong et al., 2011; Zhou et al., 2002, 2005, 2008). Geochemistry studies suggested that the Fe–Ti-oxide-bearing layered intrusions are genetically linked with high-Ti Emeishan continental flood basalts, which were generated by the partial melting of a mantle plume head with a minor sub-continental lithospheric mantle overprint (Qi and Zhou 2008; Song et al., 2009; Zhou et al., 2008).

Despite the former investigations, no consensus has been reached on the formation mechanism of thick Fe–Ti oxide layers in these intrusions and related magma chamber processes, such as why the thick Fe–Ti oxide ore layers usually present in the lower parts of the layered intrusions when compared with the Skaergaard intrusion and the Bushveld Complex (Eales and Cawthorn, 1996; McBirney, 1996; Wager and Brown, 1968)? Whether the thick oxide stratiforms were formed by fractional crystallization (Wager and Brown, 1968), liquid immiscibility (Philpotts, 1982; Reynolds, 1985) or by magma mixing (Cawthorn and McCarthy, 1981; Harney et al., 1990) is still debated.

The Baima intrusion is one of the largest layered intrusions in the ELIP. Detailed petrology, mineralogy and chemical studies indicate that the formation of the lithologic sequences in this intrusion was

* Corresponding author at: State Key Laboratory of Ore Deposit Geochemistry, Institute of Geochemistry, Chinese Academy of Sciences, 46th Guanshui Road, Guiyang 550002, China. Tel.: +86 851 5895538; fax: +86 851 5891664.
E-mail address: songxieyan@vip.gyig.ac.cn (X.Y. Song).

0169-1368/$ – see front matter © 2012 Elsevier B.V. All rights reserved.
http://dx.doi.org/10.1016/j.oregeorev.2012.09.003

constrained by fractional crystallization. This paper uses MELTS algorithm (Ghiorso and Sack, 1995) to model the fractional crystallization processes and formation of the thick Fe–Ti oxide layers in the Baima intrusion. The results lead us to maintain that fractional crystallization in a magma system closed to oxygen at depth will increase iron and titanium contents and fO_2 condition in the residual magma. Frequent recharges of such Fe–Ti enriched fractionated magma and early fractional crystallization of Fe–Ti oxides are the key factors forming the thick Fe–Ti oxide deposit at the base of the Baima layered intrusion.

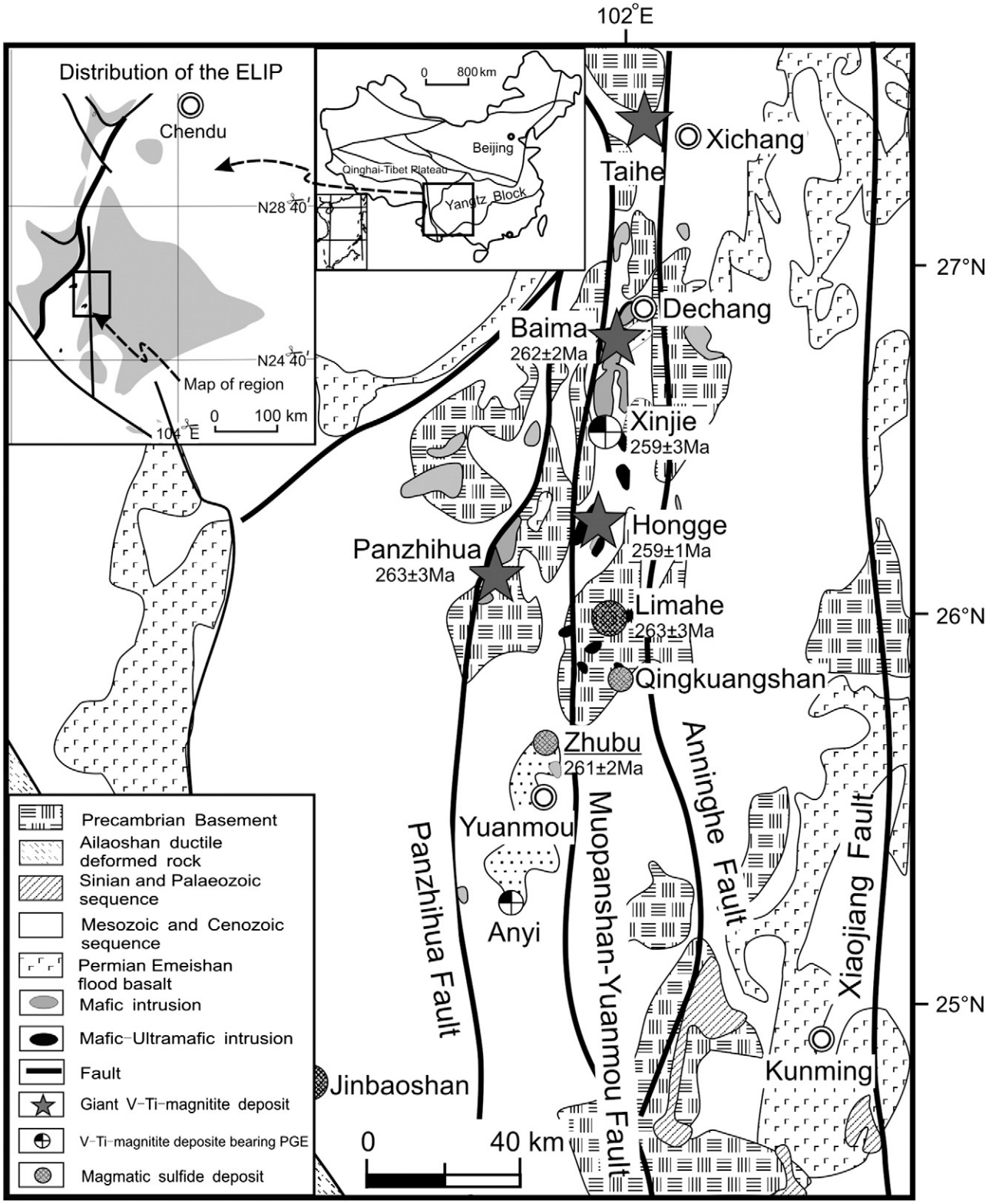

Fig. 1. Regional geological map of the central ELIP, showing the distribution of layered mafic–ultramafic intrusions that host giant Fe–Ti–V oxide deposits (modified after Song et al., 2009).

2. Geological background

The ELIP covers an area more than 5×10^5 km^2 in southwestern China and northern Vietnam and is derived from a Late Permian mantle plume (Chung and Jahn, 1995; He et al., 2003, 2007; Song, et al., 2001, 2004; Xiao et al., 2004; Xu et al., 2001; Zhou et al., 2002 and references there in). It consists of the Emeishan continental flood basalts, mafic–ultramafic intrusions, and related felsic intrusions. The Emeishan basalts in the central ELIP include upper high-Ti (HT) basalts (Ti/Y > 500) and lower low-Ti (LT) basalts (Ti/Y < 500) (He et al., 2010; Xiao et al., 2004; Xu et al., 2001). Whereas, in the outer zone of the ELIP the Emeishan basalts are mainly high-Ti basalts (Chen et al., 2010; Song et al., 2009; Xiao et al., 2004; Xu et al., 2001).

In the central ELIP, several mafic–ultramafic layered intrusions host the most economically important Fe–Ti oxide deposits in China. These layered intrusions distributed in an N–S trending area (Panxi area), and include from north to south: Taihe, Baima (262 ± 2 Ma, Zhou et al., 2008), Xinjie (259 ± 3 Ma, Zhou et al., 2002), Hongge (259 ± 1.3 Ma, Zhong and Zhu, 2006) and Panzhihua (263 ± 3 Ma, Zhou et al., 2005). They are subdivided into mafic layered intrusions comprising predominantly gabbro, olivine gabbro and troctolite (such as the Taihe, Baima, Panzhihua) and mafic–ultramafic intrusions comprising gabbro, clinopyroxenite and olivine clinopyroxenite (e.g. Hongge and Xinjie) (Fig. 1) (PXGU, 1984).

3. Petrography of the Baima intrusion

The Baima mafic layered intrusion is located in the central part of the Panxi area, SW China (Fig. 1). The N–S striking intrusion is ~24 km long and ~2 km wide, dips to the west in 50–70°, and is emplaced into the Sinian metamorphic sandstone, phyllite, slate and marble (Fig. 2). After emplacement, the Baima intrusion was surrounded and cut by ~259 Ma syenitic intrusions and dykes (PXGU, 1984). In addition, several NW–SE-trending faults separate the Baima intrusion into five segments, including Xiajiaping, Jijiping, Tianjiacun, Qinggangping and Mabinglang (Fig. 2). Along the strike, the Baima intrusion shows a thickness gradation from a more primitive facies in the north to a more evolved thinner facies in the south. The magnetite ore reserve of Baima intrusion is 1497 Mt (million ton) with mean grades of ~26% total Fe, ~7% TiO_2 and ~0.21% V_2O_5 (Ma et al., 2003).

Based on lithologic textures and mineral assemblages, the Baima layered intrusion is divided into a Fe–Ti–V oxide-mineralized lower zone (LZ) and an apatite-bearing upper zone (UZ) (Fig. 3). The boundaries between the LZ and the UZ have been defined by remarkable increases of plagioclase and decreases of Fe–Ti oxide (titanomagnetite + ilmenite).

The LZ is further subdivided into LZa and LZb, based on modal proportions of Fe–Ti oxides and silicate minerals (Fig. 3). LZa is dominated by thick medium-grained densely disseminated and disseminated oxide ores, intergrown with 2–10 mm thick barren troctolite (with <5 modal% Fe–Ti oxide). The densely disseminated oxide ores typically contain 45–60 modal% Fe–Ti oxides, 25 to 40% olivine, <20% plagioclase, and <15% clinopyroxene. The disseminated oxide ores generally contain 20–45 modal% Fe–Ti oxides, 30 to 40% olivine, <20% plagioclase, and <15% clinopyroxene. The troctolites consist of 20–30% olivine, 35–55% plagioclase, <15% clinopyroxene, and <20% Fe–Ti oxides (Fig. 3). These rocks are characterized by higher olivine/clinopyroxene ratios than the LZb (Fig. 3). LZb mainly consists of disseminated ore and

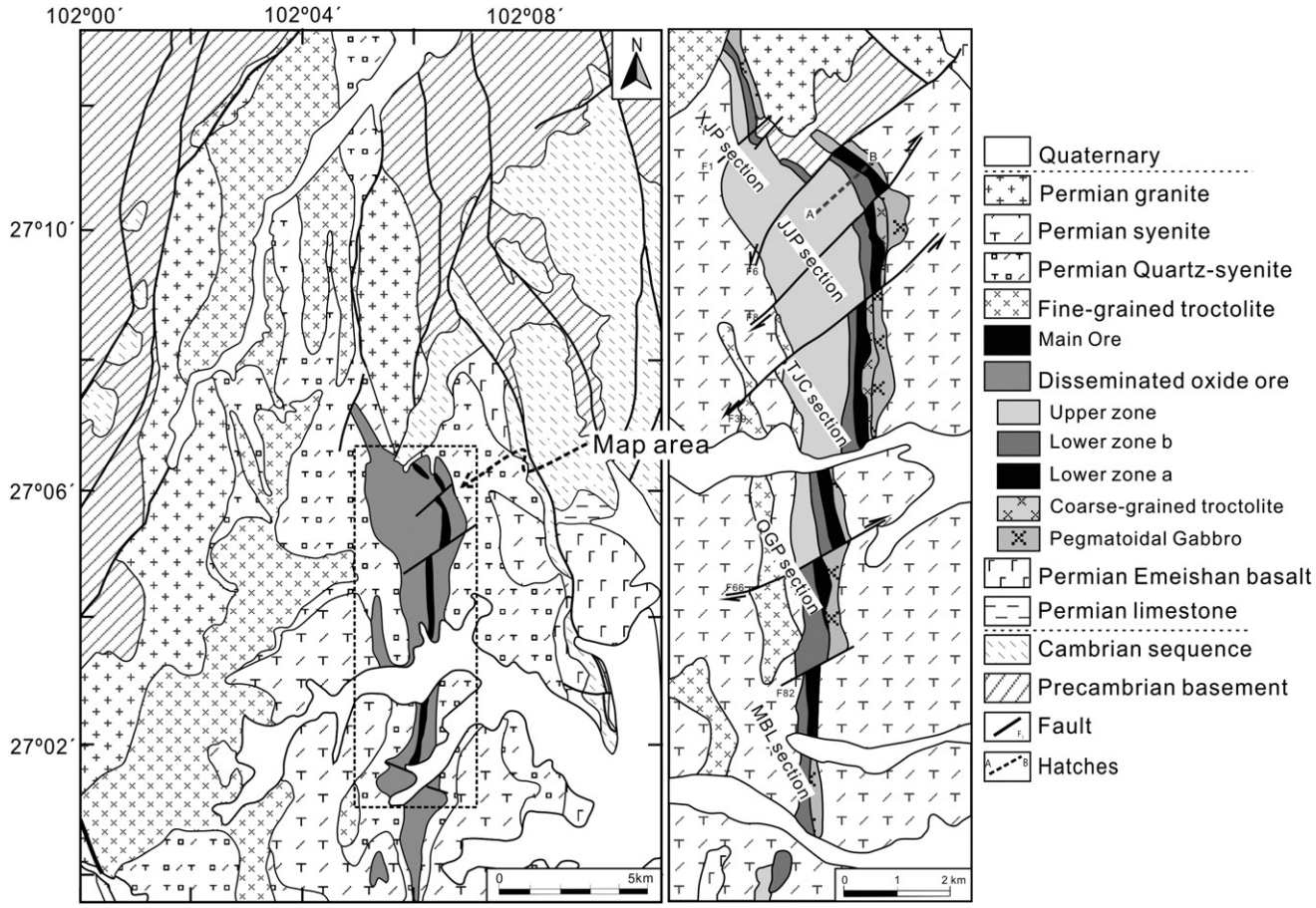

Fig. 2. Simplified regional geological map of the Baima layered intrusion (modified after PXGU, 1984). Section name: XJP (Xiajiaping), JJP (Jijiping), TJC (Tianjiacun), QGP (Qinggangping), MBL (Mabinlang).

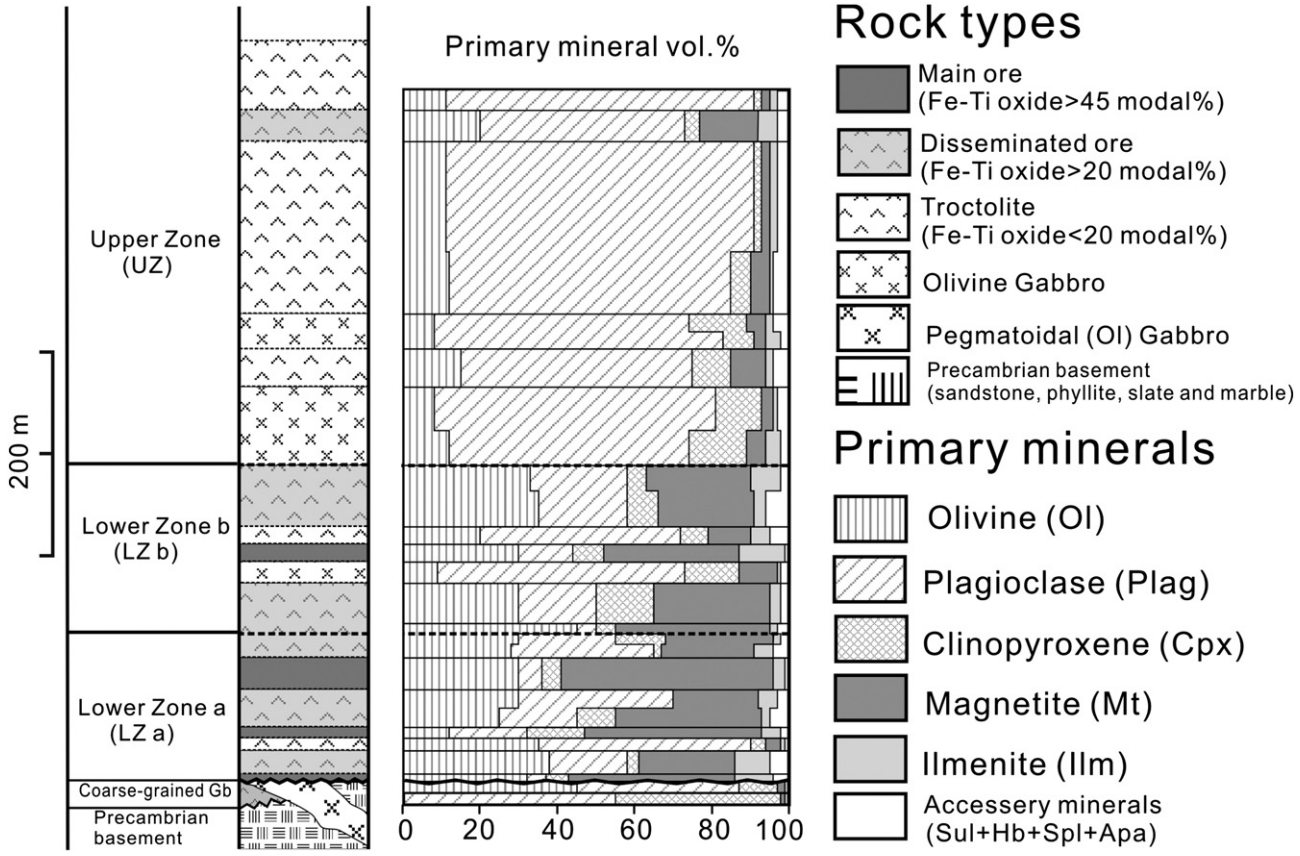

Fig. 3. Stratigraphic column of the Baima layered intrusion, showing the subdivision and proportions of minerals. Sul = sulfide, Hb = hornblende, Spl = spinel, Apa = apatite.

troctolite with interlayer of olivine gabbro. It is remarkable for rhythmic layering (generally 10–20 cm thick) composed of magnetite-rich troctolite layer at the base and troctolite and olivine gabbros on the top. The magnetite-rich layers typically have sharp bases, but gradational tops. In this study, we define rocks containing 45–60 modal% Fe–Ti oxides as the main ore; those contain <20% Fe–Ti oxides are denominated as barren troctolite; and rocks with between 20 and 45% Fe–Ti oxide are called disseminated oxide ore (Fig. 3).

Olivine represents slightly elongated oval grains ranging from 0.5 to 2.5 mm in diameter (Fig. 4a). Some of the olivine grains in the main ore enclose Fe–Ti oxide and/or plagioclase grains (Fig. 4f, g). The plagioclase crystals are generally elongated in size from 1 to 6 mm (Fig. 4b, c, d), and have a preferred orientation in the plane of the layering. Small euhedral plagioclase crystals are enclosed by olivine or clinopyroxene (Fig. 4f). The clinopyroxene grains contain numerous, small, regularly oriented plates of ilmenite, and commonly host euhedral or irregular Fe–Ti oxide inclusions (Fig. 4e). The modal abundance of the silicate and oxide minerals shows a systematic variation from magnetite layer to troctolite, and sharply decreases from LZ to UZ (Fig. 3). The inversed variation between modal abundance of plagioclase and Fe–Ti oxide shows a strong density sorting effect.

The titanomagnetites both in magnetite layer and barren troctolite have experienced significantly sub-solidus re-equilibration as represented by abundant exsolution lamellae of ilmenite and hercynite. In the main ore, the titanomagnetite crystals isolate the silicate grains, and display 120° triple junctions (Fig. 4h); in the barren troctolite or gabbro, they generally occupy the interstitial space between the major silicates. Titanomagnetite inclusions hosted in olivine or plagioclase grains have relatively high Cr contents than those interstitial grains (Table 4). Compared with the titanomagnetite, most of the ilmenite grains are interstitial and have rarely subsolidus exsolution lamellae. Accessory minerals in LZa and LZb include brown hornblende (<2%) and minor sulfides (dominated by pyrrhotite and pentlandite) and hercynite.

The upper zone (UZ) with a thickness ~1060 m shows relatively homogeneous in lithology, and mainly consists of barren troctolite and olivine gabbro. Compared with LZ, most rocks within the UZ contain >50% plagioclase but <10% Fe–Ti oxides (sometimes up to 15%), and with variable amounts of olivine and clinopyroxene. The appearance of apatite (up to 2%) is also a distinguishable feature of the UZ (Fig. 3).

The textural relationship between the minerals in the Baima intrusion indicates that general crystallization sequence order is: high-Cr titanomagnetite → plagioclase + High-Cr titanomagnetite → olivine + Fe-Ti oxide +plagioclase ± High-Cr titanomagnetite → Plagioclase + olivine + Fe-Ti oxide + clinopyroxene → plagioclase + olivine + Fe-Ti oxide + clinopyroxene + apatite.

4. Sampling and analytical techniques

Our samples were mainly collected from the LZa to the middle of UZ at the Jijiping section. Modal mineralogy and the stratigraphic position of samples from the Jijiping section are displayed in Fig. 3.

Major oxide analysis was completed at the Analytical Centre of the Metallogenic Geology Bureau of Southwestern China, Chengdu. For the major elements, SiO_2 and H_2O were determined by gravimetric method, TiO_2 and P_2O_5 by spectrophotometry, Al_2O_3, Fe_2O_3, FeO, V_2O_5 and CO_2 by titrimetry, and MnO, MgO, CaO, Na_2O, and K_2O by atomic absorption spectrometry. The analytical uncertainty is usually <5% except for H_2O and CO_2. Cr contents were analyzed, as trace element, using a Perkin-Elmer EIAN DRC II ICP-MS at the Institute of Geochemistry, Chinese Academy of Sciences. 50 mg of powder for each sample was dissolved using the method described by Qi et al. (2000) and 500 mg/ml Rh was used as an internal standard. The nebulized solutions were analyzed using a VG Plasma-Quad Excell

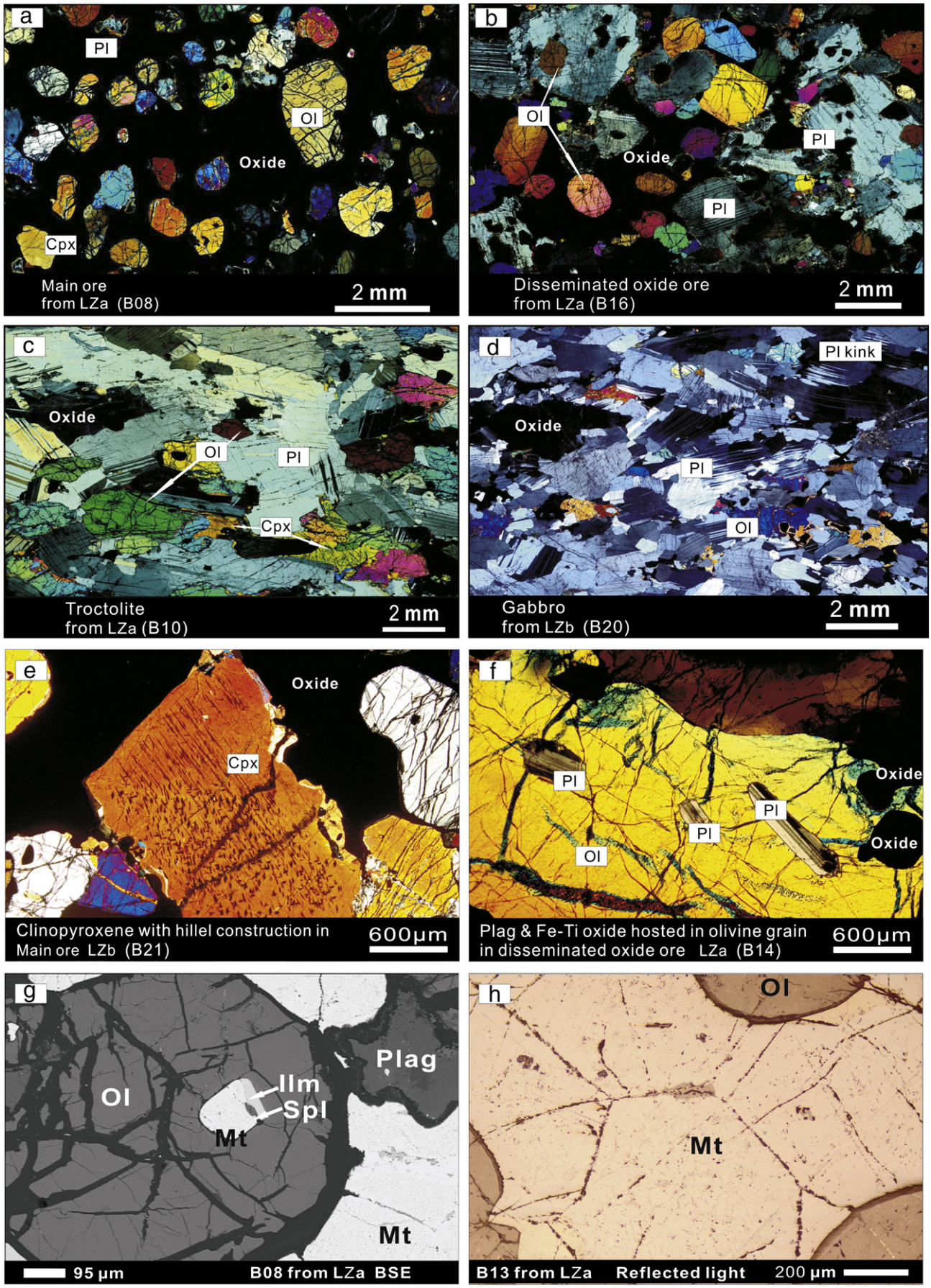
a
Pl
Ol
Oxide
Cpx
Main ore
from LZa (B08)
2 mm
b
Ol
Oxide
Pl
Pl
Disseminated oxide ore
from LZa (B16)
2 mm
c
Oxide
Ol
Pl
Cpx
Troctolite
from LZa (B10)
2 mm
d
Pl kink
Oxide
Pl
Ol
Gabbro
from LZb (B20)
2 mm
e
Oxide
Cpx
Clinopyroxene with hillel construction in
Main ore LZb (B21)
600μm
f
Pl
Oxide
Pl
Pl
Oxide
Ol
Plag & Fe-Ti oxide hosted in olivine grain
in disseminated oxide ore LZa (B14)
600μm
g
Plag
Ol
Ilm
Spl
Mt
Mt
95 μm
B08 from LZa BSE
h
Ol
Mt
B13 from LZa Reflected light
200 μm

Table 1
Whole rock major oxide concentrations in rocks of the Jijiping section of the Baima intrusion, SW China.

Zone	Sample	Rock	Height (m)	SiO_2 (wt.%)	TiO_2 (wt.%)	Al_2O_3 (wt.%)	Fe_2O_3 (wt.%)	FeO (wt.%)	MnO (wt.%)	MgO (wt.%)	CaO (wt.%)	K_2O (wt.%)	Na_2O (wt.%)	P_2O_5 (wt.%)	V_2O_5 (wt.%)	LOI (wt.%)	Total (wt.%)	Cr (ppm)
Upper zone	B39	Diss-Ore	700	38.75	4.19	20.05	9.36	11.25	0.15	3.55	7.85	0.25	2.91	0.09	0.16	1.01	99.57	25.9
	B38	Troctolite	600	46.70	1.66	22.82	3.61	6.23	0.10	3.86	9.72	0.31	3.53	0.18	0.06	0.85	99.63	2.19
	B37	Troctolite	525	45.68	1.83	22.51	3.95	6.85	0.10	3.78	9.43	0.29	3.33	0.15	0.07	1.69	99.66	10.5
	B32	Gabbro	500	44.25	2.63	22.46	5.23	7.91	0.11	2.85	9.36	0.29	3.37	0.14	0.10	0.99	99.68	17.3
	B31	Gabbro	495	46.61	1.66	22.47	3.67	6.33	0.11	4.02	9.86	0.31	3.43	0.20	0.06	0.91	99.63	9.72
	B30	Troctolite	465	42.72	2.62	20.06	4.80	10.33	0.14	5.35	8.52	0.31	2.95	0.14	0.10	1.60	99.65	29.3
	B29	Gabbro	415	44.26	2.29	19.98	4.92	8.58	0.13	5.32	9.50	0.26	3.00	0.11	0.09	1.25	99.69	4.90
	B28	Ol-Gabbro	385	45.59	1.90	20.70	3.70	7.66	0.12	4.96	10.04	0.34	3.12	0.18	0.07	1.26	99.64	1.05
Lower zone b (LZb)	B27	Diss-Ore	355	25.11	6.53	8.39	16.42	22.99	0.33	12.49	3.34	0.15	0.75	0.08	0.27	3.02	99.88	43.1
	B25	Diss-Ore	325	21.05	7.02	4.87	21.85	21.59	0.37	14.73	2.19	0.05	0.31	0.08	0.30	5.31	99.70	59.5
	B24	Troctolite	295	36.37	3.88	15.70	9.72	13.63	0.20	7.61	6.68	0.31	2.09	0.10	0.16	3.38	99.82	23.6
	B21	Main Ore	283	16.32	9.57	4.97	25.61	26.17	0.39	11.60	1.99	0.04	0.24	0.06	0.37	2.32	99.65	108
	B20	Gabbro	267	39.94	3.10	16.48	6.53	12.75	0.19	8.51	8.06	0.24	2.40	0.10	0.13	1.09	99.51	21.6
	B19	Diss-Ore	217	26.79	5.94	7.15	15.89	20.87	0.34	13.25	4.76	0.09	0.61	0.10	0.25	3.71	99.75	46.6
Lower zone a (LZa)	B18	Diss-Ore	202	16.95	8.21	3.99	22.23	26.42	0.39	14.07	1.17	0.03	0.17	0.07	0.36	5.58	99.64	96.3
	B17	Diss-Ore	193	22.82	7.42	5.33	19.59	23.01	0.37	13.36	4.41	0.05	0.30	0.07	0.31	2.76	99.81	58.9
	B16	Diss-Ore	183	30.40	4.93	12.76	11.84	19.48	0.26	10.68	4.89	0.27	1.26	0.06	0.21	2.59	99.64	1544
	B15	Main Ore	158	12.80	9.83	3.73	28.20	26.88	0.40	12.17	0.75	0.01	0.11	0.07	0.43	4.51	99.88	153
	B14	Diss-Ore	138	28.60	5.34	12.29	14.84	19.18	0.28	10.38	4.75	0.24	1.16	0.09	0.26	2.39	99.79	2380
	B13	Diss-Ore	113	17.00	8.60	5.26	21.68	28.00	0.38	12.63	1.64	0.04	0.30	0.07	0.36	3.93	99.89	158
	B11	Main Ore	103	13.22	10.4	7.52	30.02	25.01	0.35	6.55	3.62	0.08	0.30	0.06	0.45	2.15	99.68	4451
	B10	Troctolite	95	39.43	2.37	16.39	6.16	13.20	0.21	11.46	6.89	0.27	1.98	0.06	0.10	1.10	99.62	705
	B09	Diss-Ore	65	20.98	7.71	8.00	19.90	24.66	0.33	10.91	3.22	0.09	0.65	0.07	0.32	2.98	99.81	107
	B08	Main Ore	60	18.35	8.79	4.86	21.54	25.92	0.37	13.44	2.45	0.03	0.20	0.06	0.32	3.52	99.86	92.6
Basal gabbro	B02	Coarse-Gb	15	47.53	0.71	10.56	1.90	8.47	0.19	13.47	14.05	0.13	1.24	0.04	0.03	1.44	99.77	318
	B01	Coarse-Gb	5	49.07	0.96	12.58	2.01	4.96	0.14	9.58	16.25	0.59	1.37	0.05	0.05	2.16	99.76	470

Coarse-Gb = coarse-grained gabbro; Diss-Ore = disseminated oxide ore; LOI = loss on ignition.

Table 2
Analysis of olivine (wt.%) in the Jijiping section of the Baima intrusion.

Zone	Sample	Rock	Height (m)	N	Na_2O	MgO	Al_2O_3	SiO_2	CaO	TiO_2	Cr_2O_3	MnO	FeO	NiO	Total	Fo
Upper zone	B39	Diss-Ore	700	6	0.00	32.14	0.00	37.94	0.04	0.03	0.00	0.50	29.02	0.01	99.67	67
	B38	Troctolite	600	10	0.02	30.75	0.00	37.60	0.03	0.01	0.01	0.50	31.16	0.01	100.10	64
	B37	Troctolite	525	6	0.00	29.06	0.00	36.14	0.03	0.01	0.00	0.53	32.98	0.01	98.76	61
	B32	Gabbro	500	7	0.00	25.71	0.01	36.14	0.04	0.01	0.01	0.60	37.03	0.02	99.58	55
	B31	Gabbro	495	6	0.00	30.42	0.02	36.78	0.02	0.00	0.00	0.56	31.45	0.01	99.27	63
	B30	Troctolite	465	6	0.00	29.20	0.00	36.74	0.02	0.02	0.01	0.51	32.77	0.02	99.29	61
	B29	Gabbro	415	9	0.00	29.09	0.00	36.94	0.02	0.01	0.01	0.53	31.60	0.02	98.22	62
	B28	Ol-Gabbro	385	10	0.01	28.96	0.03	37.42	0.02	0.01	0.03	0.53	33.29	0.03	100.33	61
Lower zone b (LZb)	B25	Diss-Ore	325	7	0.01	34.92	0.00	38.22	0.08	0.02	0.01	0.44	25.80	0.01	99.51	71
	B24	Troctolite	295	6	0.00	33.15	0.00	37.90	0.04	0.01	0.00	0.47	28.04	0.01	99.63	68
	B21	Main ore	282	6	0.02	35.86	0.00	38.69	0.06	0.03	0.01	0.39	24.56	0.02	99.64	72
	B20	Gabbro	266	9	0.02	31.88	0.01	38.22	0.06	0.03	0.01	0.45	28.80	0.02	99.51	66
	B19	Diss-Ore	216	6	0.01	34.24	0.00	39.15	0.06	0.03	0.01	0.43	26.10	0.02	100.05	70
Lower zone a (LZa)	B18	Diss-Ore	202	4	0.00	36.35	0.00	38.27	0.06	0.01	0.01	0.40	23.91	0.01	99.03	73
	B17	Diss-Ore	192	6	0.00	35.53	0.00	38.12	0.05	0.01	0.00	0.40	24.96	0.01	99.08	72
	B16	Diss-Ore	182	7	0.00	32.75	0.00	37.22	0.03	0.01	0.01	0.44	28.36	0.03	98.86	67
	B15	Main ore	157	5	0.02	36.95	0.02	38.73	0.05	0.05	0.01	0.31	23.00	0.03	99.15	74
	B14	Diss-Ore	137	6	0.00	34.65	0.02	37.07	0.05	0.00	0.00	0.42	26.16	0.05	98.42	70
	B13	Diss-Ore	113	6	0.00	36.08	0.01	38.05	0.06	0.02	0.01	0.41	24.31	0.03	98.97	73
	B11	Main ore	102	6	0.01	36.91	0.00	39.29	0.06	0.02	0.02	0.36	22.97	0.03	99.68	74
	B10	Troctolite	95	6	0.00	32.62	0.01	38.66	0.04	0.01	0.00	0.49	28.94	0.05	100.82	67
	B09	Diss-Ore	65	9	0.00	35.67	0.01	39.02	0.06	0.02	0.01	0.41	24.55	0.03	99.79	72
	B08	Main ore	60	7	0.01	35.32	0.01	38.02	0.08	0.03	0.01	0.41	25.17	0.02	99.08	72
Basal gabbro	B02	Coarse-Gb	15	9	0.00	31.10	0.03	38.38	0.04	0.02	0.00	0.50	30.14	0.05	100.25	65

Rock name abbreviations as Table 1. N = number of analysis. Fo = forsterite percentage of olivine.

ICP-MS. We used standard additions, pure elemental standards for external calibration, and standards MSAN, OU-6, AMH-1, and GBPG-1 as reference materials. Accuracy and precision of the ICP-MS analyses are estimated to be better than 5%. Major element compositions and Cr contents are listed in Table 1.

Electron microprobe analyses of olivine and plagioclase in this study were performed using the EMPA-1600 electron microprobe at Institute of Geochemistry, Chinese Academy of Sciences, Guiyang. Accelerating voltage is 25 kV and a beam current of 10 nA was used. The detection limit for these elements under such conditions is 0.01 wt.%.

Fig. 4. Rock textures in the Baima intrusion (crossed polars, BSE and reflected light). (a) Main ore (B08) from LZa; (b) disseminated oxide ore (B16) from LZa; (c) troctolite (B10) from LZa; (d) medium-coarse grained gabbro (B20) from LZb; (e) clinopyroxene with hillel structure in the main ore in LZb (B21); (f) olivine grain host plagioclases and Fe–Ti oxide grains in the disseminated oxide ore in LZa (B14); (g) euhedral magnetite hosted in olivine, with ilmenite and spinel exsolution. In the main ore (B08) of the LZa (BSE). (h) Polygonal grains of magnetite with straight distinct boundaries that are in contact through ~120° interfacial angles in the disseminated oxide ore (B13) of LZa (reflected light). Ol = olivine; Cpx = clinopyroxene; Pl/Plag = plagioclase; oxide = Fe–Ti oxide; Mt = magnetite; Ilm = ilmenite; Spl = hercynite.

Table 3
Analysis of plagioclase (wt.%) in the Jijiping section of the Baima intrusion.

Zone	Sample	Rock	Height (m)	N	Na_2O	Al_2O_3	SiO_2	K_2O	CaO	TiO_2	FeO	Total	An
Upper zone	B39	Diss-Ore	700	6	4.59	28.18	54.44	0.34	11.52	0.05	0.35	99.47	58
	B38	Troctolite	600	10	4.56	28.32	55.73	0.34	11.39	0.08	0.24	100.65	58
	B37	Troctolite	525	6	4.91	27.79	55.45	0.21	11.18	0.06	0.20	99.81	56
	B32	Gabbro	500	7	4.84	28.08	54.66	0.18	11.19	0.07	0.25	99.49	56
	B31	Gabbro	495	6	4.67	28.18	54.78	0.21	11.65	0.10	0.25	99.85	58
	B30	Troctolite	465	6	4.84	28.46	53.54	0.15	11.25	0.08	0.23	98.55	56
	B29	Gabbro	415	9	4.67	27.94	55.05	0.31	10.95	0.08	0.23	99.22	56
	B28	Ol-Gb	385	10	4.85	27.98	56.36	0.20	11.21	0.06	0.27	100.94	56
Lower zone b (LZb)	B25	Diss-Ore	325	7	4.85	27.98	56.36	0.20	11.21	0.06	0.27	99.53	56
	B24	Troctolite	295	6	4.64	28.39	55.10	0.29	11.53	0.08	0.27	100.28	58
	B21	Main ore	282	6	4.57	28.32	55.66	0.15	11.75	0.09	0.18	100.72	59
	B20	Gabbro	266	9	4.56	28.06	55.33	0.36	11.41	0.06	0.32	100.11	58
	B19	Diss-Ore	216	6	4.60	28.16	55.29	0.20	11.59	0.07	0.24	100.15	58
Lower zone a (LZa)	B18	Diss-Ore	202	4	4.68	28.41	54.46	0.13	11.59	0.10	0.13	100.06	58
	B17	Diss-Ore	192	6	4.71	28.61	54.45	0.15	11.50	0.06	0.14	99.63	57
	B16	Diss-Ore	182	7	4.15	29.07	53.92	0.08	12.68	0.09	0.23	100.23	63
	B15	Main ore	157	5	4.51	28.55	55.03	0.10	11.67	0.12	0.05	100.04	59
	B14	Diss-Ore	137	6	3.95	29.66	51.77	0.10	13.12	0.09	0.23	98.90	65
	B13	Diss-Ore	113	6	4.56	28.07	55.05	0.14	11.39	0.09	0.11	99.41	58
	B11	Main ore	102	6	3.63	29.78	53.84	0.10	13.57	0.04	0.21	101.17	67
	B10	Troctolite	95	6	3.72	28.94	54.67	0.33	12.97	0.05	0.43	101.12	66
	B09	Diss-Ore	65	9	4.73	28.41	55.56	0.05	11.48	0.07	0.15	100.44	57
	B08	Main ore	60	7	4.54	28.80	55.66	0.05	11.57	0.07	0.12	100.81	58
Basal gabbro	B02	Coarse-Gb	15	9	4.30	28.66	54.80	0.14	12.07	0.08	0.29	100.35	61
	B01	Coarse-Gb	5	6	3.61	28.82	53.11	0.78	12.26	0.09	0.34	99.04	66

Rock name abbreviations as Table 2. N = number of analysis. An = anorthite percentage of plagioclase.

Analytical reproducibility was within 2%. The accuracy of the analysis was monitored using mineral standards: pyrope for Mg, Al, Cr and Mn, rutile for Ti, magnetite for Fe and olivine for Ni. Our estimation includes more than 400 grains. The average compositions of olivine and plagioclase in each sample are listed in Tables 2, 3 and 4.

5. Results

Most of our samples are fresh, and with low loss-on-ignition (LOI) values (<4 wt.%, a few of them up to 6 wt.%) (Table 1). Stratigraphic variations of major elements of the Baima layered intrusion are illustrated in Fig. 5 and summarized in Table 1. Most of the major elements show wider scatter in the LZ but are relatively constant in the UZ. In the LZ, the SiO_2 and Al_2O_3 concentrations increase from main ore to troctolite or gabbro, whereas the FeO_T and TiO_2 decrease, representing strong cumulus mineral controlling trend. The Fe^{3+}/Fe^{2+} ratio shows similar variation trends from main ore to troctolite or gabbro, reflecting the variable ratio between titanomagnetite and ilmenite. Compared with the LZ, rocks in the UZ are significantly low in FeO_T, TiO_2 and MgO and high in SiO_2, Al_2O_3 and CaO contents. Contents of P_2O_5 show gradually increasing features from the LZ to the UZ. Whole-rock Cr concentration represents three abrupt reversals in the LZa, decreasing systematically from 4450 ppm at the first reversal, 2380 ppm for the second and 1544 ppm at the top of LZa. However, the general trend of whole-rock Cr content decreases upwards.

As shown in Fig. 5, the olivine forsterite (Fo) contents of the LZ range from 66 to 74, which are higher than those of the olivine of the UZ, ranging from 55 to 67 (Table 2). The plagioclase anorthite (An) contents in the LZb (56–59) are comparable with those in the UZ (56–58) but lower than those in the LZa (57–67) (Table 3, Fig. 5). In the LZ, variation of Fo contents of the olivine is perfectly consistent with the variation of the whole-rock Fe^{3+}/Fe^{2+} ratios (Fig. 5). The olivine crystals of the main ores usually have higher Fo than those of the disseminated oxide ores and troctolites. In contrast, An contents of the plagioclase represented three remarkable reverses in the LZa, synchronous with the whole-rock Cr contents (Fig. 5), but appear to have no linear relationship with whole-rock Fe^{3+}/Fe^{2+} ratio. Except for four remarkable reversals in An content, samples from the Baima intrusion have higher plagioclase An and olivine Fo contents, but similar fractionation trend for the upper magnetite-bearing zone of the Skaergaard intrusion and the Bushveld Complex (Fig. 6).

Ilmenite exsolution lamellae in magnetite are common in the Baima intrusion and other layered intrusions in the ELIP (Bai et al., 2012; Pang et al., 2008a). Hence, the original oxide element compositions such as MgO, TiO_2, and MnO were changed during the subsolidus re-equilibration and exsolution process. Compositions of the magnetite of the main ore, disseminated oxide ore and troctolite at the base of the LZa have been measured (Table 4). The magnetites enclosed in olivine crystals in these three samples have higher Cr_2O_3 contents (0.10–2.09 wt.%) than the cumulate magnetite grains (Cr_2O_3 = 0.01–1.23 wt.%) (Table 4). The Cr_2O_3 contents of the cumulate magnetite grains of the troctolite (B10) (0.94–1.23 wt.%) are distinctly higher than those of the disseminated oxide ores (B08 and B09). This is consistent with the whole rock Cr content variation of these samples and indicates that the magnetite is the dominant phase containing Cr. Three single magnetite grains in the sample B08 are extremely low in MgO and TiO_2 probably because of the late alteration, which is indicated by high LOI (3.52 wt.%, Table 1).

6. Discussion

Experimental studies have indicated that liquid immiscibility in silicate melts occurs under high fO_2, and most of the Fe-rich immiscible liquid component is not only high in Fe_2O_3 and TiO_2, but also high in P_2O_5 and REE (Naslund, 1983; Philpotts, 1982). Immiscibility between Fe-rich- and Si-rich-liquids was employed to interpret the formation of the magnetite ore layers within diorite of the upper zone of the Bushveld Complex and the Skaergaard intrusion (Humphreys, 2011; VanTongeren and Mathez, 2012). This means that such immiscibility might occur in very late stage of magma evolution.

However, the Fe–Ti oxide-rich layers occur within troctolites and gabbros in the LZ of the Baima layered intrusions. They display sharp bases by abruptly high proportion of magnetite and ilmenite, which decrease upwards. Whereas, the proportion of plagioclase increases gradually (Fig. 3). Such gradual changes would not be expected at the

Table 4
Compositions of titanomagnetite from the Baima layered intrusion. Italics represent data from titanomagnetite inclusions hosted in olivine.

Sample	B8-1	B8-2	B8-3	B8-4	B8-5	B8-6	B8-7	B8-8	B9-1	B9-2	B9-3	B9-4	B9-5	SB9-6	B9-7	B9-8	B10-1	B10-2	B10-3	B10-4	B10-5	B10-6	B10-7	B10-8	B10-9
Type	Inclusion	Single	Single	Single	Single	Single	Single	Single	Inclusion	Single	Single	Single	Single	Single	Single	Single	Inclusion	Single	Single	Single	Single	Single	Single	Single	Single
Main ore (wt.%)									Diss-Ore								Troctolite								
MgO	*1.16*	0.07	0.67	1.65	0.01	2.12	1.38	0.31	*1.39*	1.39	2.07	1.17	1.51	1.29	1.35	0.48	*0.51*	0.46	0.88	0.44	0.72	0.08	0.44	0.63	0.62
Al_2O_3	*1.14*	0.93	1.26	3.55	0.25	4.18	2.54	3.47	*3.72*	3.73	5.67	3.06	3.79	3.74	3.32	2.38	*2.58*	1.13	3.86	0.69	2.32	0.48	1.02	2.04	2.23
TiO_2	*12.07*	0.02	10.69	11.74	0.96	11.13	20.68	16.42	*8.08*	7.69	9.93	8.76	9.27	7.93	7.82	13.44	*8.67*	5.02	3.10	8.08	5.44	1.24	4.45	4.06	5.45
Cr_2O_3	*0.15*	0.01	0.04	0.06	0.00	0.06	0.06	0.04	*0.10*	0.06	0.06	0.04	0.07	0.08	0.08	0.03	*2.09*	1.07	1.04	1.18	1.23	0.94	1.17	1.21	1.15
MnO	*0.54*	0.00	0.43	0.39	0.00	0.48	0.79	0.66	*0.35*	0.28	0.52	0.41	0.43	0.36	0.38	0.45	*0.28*	0.15	0.11	0.23	0.16	0.05	0.16	0.16	0.19
FeO	*28.63*	30.66	29.50	28.43	30.87	27.86	28.79	29.79	*28.90*	28.91	28.86	28.84	28.70	28.89	28.81	30.05	*29.95*	29.89	30.23	29.79	29.50	30.52	29.91	30.10	29.83
Fe_2O_3	*55.49*	66.93	56.53	53.32	67.28	53.69	46.53	47.07	*56.57*	56.79	54.71	56.10	55.52	56.27	57.19	52.51	*54.33*	60.84	60.86	58.77	58.56	65.41	61.33	61.32	59.14
NiO	*0.03*	0.00	0.01	0.03	0.00	0.01	0.01	0.02	*0.01*	0.00	0.03	0.03	0.03	0.00	0.02	0.00	*0.01*	0.07	0.08	0.32	0.07	0.07	0.01	0.04	0.04
Total	*99.21*	98.62	99.12	99.16	99.36	99.53	100.78	97.78	*99.13*	98.85	101.84	98.40	99.32	98.55	98.96	99.35	*98.41*	98.63	100.15	99.50	98.00	98.80	98.48	99.56	98.65
Cations																									
Mg	*0.07*	0.00	0.04	0.09	0.00	0.12	0.08	0.02	*0.08*	0.08	0.11	0.07	0.08	0.07	0.08	0.03	*0.03*	0.03	0.05	0.03	0.04	0.00	0.03	0.04	0.04
Al	*0.05*	0.04	0.06	0.16	0.01	0.18	0.11	0.16	*0.17*	0.17	0.24	0.14	0.17	0.17	0.15	0.11	*0.12*	0.05	0.17	0.03	0.11	0.02	0.05	0.09	0.10
Ti	*0.35*	0.00	0.31	0.33	0.03	0.31	0.58	0.48	*0.23*	0.22	0.27	0.25	0.26	0.23	0.22	0.39	*0.25*	0.15	0.09	0.23	0.16	0.04	0.13	0.12	0.16
Cr	*0.00*	0.00	0.00	0.00	0.00	0.00	0.00	0.00	*0.00*	0.00	0.00	0.00	0.00	0.00	0.00	0.00	*0.06*	0.03	0.03	0.04	0.04	0.03	0.04	0.04	0.03
Mn	*0.02*	0.00	0.01	0.01	0.00	0.02	0.02	0.02	*0.01*	0.01	0.02	0.01	0.01	0.01	0.01	0.01	*0.01*	0.00	0.00	0.01	0.01	0.00	0.01	0.01	0.01
Fe^{2+}	*0.92*	1.00	0.95	0.89	1.00	0.87	0.90	0.96	*0.91*	0.91	0.87	0.92	0.90	0.92	0.91	0.96	*0.96*	0.97	0.95	0.96	0.95	0.99	0.97	0.96	0.96
Fe^{3+}	*1.60*	1.96	1.63	1.51	1.96	1.50	1.31	1.37	*1.60*	1.61	1.49	1.61	1.57	1.60	1.63	1.51	*1.57*	1.77	1.71	1.70	1.70	1.91	1.79	1.76	1.71
Ni	*0.00*	0.00	0.00	0.00	0.00	0.00	0.00	0.00	*0.00*	0.00	0.00	0.00	0.00	0.00	0.00	0.00	*0.00*	0.00	0.00	0.01	0.00	0.00	0.00	0.00	0.00
Total	*3.00*	3.00	3.00	3.00	3.00	3.00	3.00	3.00	*3.00*	3.00	3.00	3.00	3.00	3.00	3.00	3.00	*3.00*	3.00	3.00	3.00	3.00	3.00	3.00	3.00	3.00

top of the dense layer of iron-rich liquid (Cawthorn and Ashwal, 2009). Positive correlation between Fo of olivine and An of plagioclase (Fig. 6) suggests that one of the key factors controlling the formation of the Baima intrusion is fractional crystallization, rather than liquid immiscibility. Large variations in the whole-rock Cr contents and Fe^{3+}/Fe^{2+} ratio of the main and disseminated ores (Fig. 5) and variable Cr contents of the magnetite grains (Table 4) imply variation in compositions of the new magmas. Cr is highly compatible in the magnetite compared with the ilmenite ($D_{Cr}^{Mt}=50–230$; $D_{Cr}^{Ilm}=3–40$ Klemme et al., 2006; Leeman et al., 1978; Nakamura and Fujimaki, 1986), hence, the magnetite–ilmenite subsolidus re-equilibration and exsolution process would have little effect on Cr content in magnetite. The higher Cr contents of the magnetite inclusions in the olivine crystals than that of the cumulate magnetite grains indicate that the magnetite inclusions crystallized earlier than the cumulate phase (Table 4). Hence, we believe that early crystallization of Fe–Ti oxide might be a reasonable mechanism that formed the oxide-rich layers.

The geothermal modeling program MELTS was used to investigate the magmatic fractionation process of the Fe–Ti-rich magma that was produced by high-Ti picritic magma via fractional crystallization at a deep level, and the crystallization history of the thick Fe–Ti oxide ore in the shallower Baima intrusion. The most recent GUI version of the MELTS software is applicable to natural magmatic compositions (both hydrous and anhydrous), ranging from potash ankaratrites to rhyolites, and permits the calculation of crystallization paths for a wide variety of crystallization process, including fractional crystallization and system closed to oxygen (Ghiorso and Sack, 1995).

6.1. Nature of parental magma

Similarities of Sr–Nd isotopes and trace element compositions indicated that there is a genetic link between the layered intrusions and the Emeishan high-Ti basalts (Song et al., 2005; Zhou et al., 2005). Commonly occurring ilmenite exsolution lamellae in the clinopyroxene of the Baima intrusion also indicate a high-Ti parental magma. Compared with the mantle derived olivine (Fo > 89), the low Fo content (55–74) indicates that the parental magma has experienced extensively fractional crystallization before it intruded into the Baima intrusion. Further, thick Fe–Ti oxide ore in the lower part of the Baima intrusion needs a prerequisite that the magma which entered the intrusion might be saturated in Fe and Ti, so that the Fe–Ti oxides could be the early phase appearing on the liquidus. However, the processes and the mechanisms forming the Fe–Ti-rich magma are not entirely known.

6.2. Magmatic fractionation history—model from MELTS

6.2.1. Differentiation in deep magma chamber

Relatively high $\varepsilon_{Nd(t)}$ value (+1.1 to +5) and low $^{87}Sr/^{86}Sr_{(t)}=$ ~0.704–0.705 of Emeishan high-Ti basalt and the Baima intrusion illustrate that the parental magma might have experienced only a weak crustal contamination at deep levels (Xu et al., 2001; Zhou et al., 2008). Previous studies have indicated that fractional crystallization of silicate minerals in a system closed with respect to oxygen may result in oxygen fugacity increase (Byers et al., 1984; Christie et al., 1986), and this is proven as a typical plutonic tholeiitic magma differentiation trend (Carmichael, 1967; Lattard and Partzsch, 2001; Snyder et al., 1993; Toplis and Carroll, 1996). Hence, we assume that the fractional crystallization of Baima parental magma in deep-magma chamber was under a system closed to oxygen, with assumed pressure 5 kbar (~16 km) (Pang et al., 2008a), and is a water-free system. The results are shown in Table 5 and Fig. 7.

Melt inclusion data in olivine phenocrysts (with Fo = 91.71) of the high-Ti picritic basalt, in the central ELIP (Yongsheng Yunnan province) (Kamenetsky et al., 2012) have been chosen to represent the primary magma composition for the MELTS modeling. The composition is

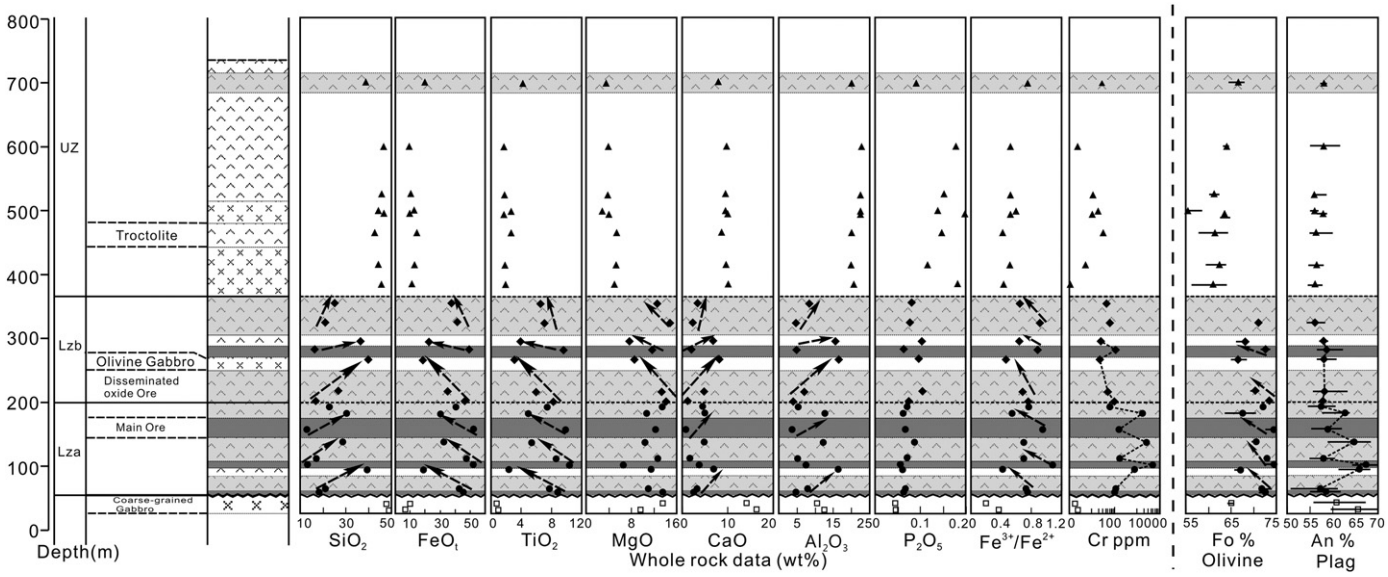

Fig. 5. Stratigraphic variations of the major oxides, Fe^{3+}/Fe^{2+} ratios, whole-rock Cr contents and the olivine and plagioclase compositions.

listed in Table 5. High Mg-number ($Mg^{\#}=74$) of the melt inclusion indicates that it probably captured from more primitive melt at high temperature (Kamenetsky et al., 2001). According to the Fe^{3+}/Fe^{2+} ratio of the melt inclusion (Kamenetsky et al., 2012), the initial fO_2 calculated by MELTS at 5 kbar under a closed to oxygen system is FMQ−0.33, the result is in accord with the fO_2 of the mantle derived magmas, i.e. below FMQ (Rhodes and Vollinger, 2005; Williams et al., 2004; Wood et al., 1990). MELTS calculation indicates that high-Fo olivine is the first phase to appear on the liquidus (Fo_{91} at 1481 °C, $\rho=3.15$), followed by minor chromite (1415 °C, $\rho=4.27$), and then orthopyroxene ($Mg^{\#}_{89}$ at 1362 °C, $\rho=3.17$) (Table 5). Crystallization of these minerals gives rise to a residual magma that is clearly gradually enriched in SiO_2, FeO_T, TiO_2, and Al_2O_3 (Fig. 7). When the temperature reaches 1285 °C, the appearance of clinopyroxene ($Mg^{\#}_{84}$, $\rho=3.20$) leads to a rapid decrease of CaO in the residual magma. By 1185 °C, there are about 16.6 wt.% olivine, 11.4 wt.% orthopyroxene, 1.0 wt.% chromite and 32.1% clinopyroxene have been removed due to fractional crystallization. As a result, the FeO_T and TiO_2 contents in the residual liquid increase to 17.55 wt.% and 4.93 wt.% respectively (Fig. 7), and the fO_2 elevates to 0.56 units above FMQ. Toplis and Carroll (1995) showed experimentally that liquid similar to the tholeiitic basalt requires at least 55% crystal fractionation before magnetite appears on the liquidus. MELTS calculation gives a similar result that after nearly 61% fractional crystallization of silicate minerals may deduce an iron and titanium rich residual magma from normal mantle-derived picritic basalt. The following crystallizing phases are plagioclase (An = 59) at 1182 °C and titanomagnetite at 1167 °C, respectively. It is noticeable that the olivine Fo content ($Fo_{max}=74$) of the Baima intrusion is much lower than those crystallized at 5 kbar (Fo = 91–86) (Table 5). This implies that the Baima intrusion is the result of crystallization of evolved magma rather than the primary magma. There is not a single complementary mafic/ultramafic cumulus, which can be equated with the evolution of the Baima magma. However, when compared with the accumulated composition sequences from chromium-rich spinel to Fe–Ti rich end member, which are reported by Scoon and Eales (2002) in Bushveld Complex, we consider that such complementary mantle-derived mafic/ultramafic cumulus was probably in a deep chamber, whereas, the evolved iron-rich residual magma was intruded into the shallower Baima magma chamber, or erupted to form the high-Ti Emeishan flood basalts with as high as ~16 wt.% $Fe_2O_{3(T)}$ and 4.5 wt.% TiO_2, but low in Cr and Ni (Song et al., 2001, 2008; Xu et al., 2001).

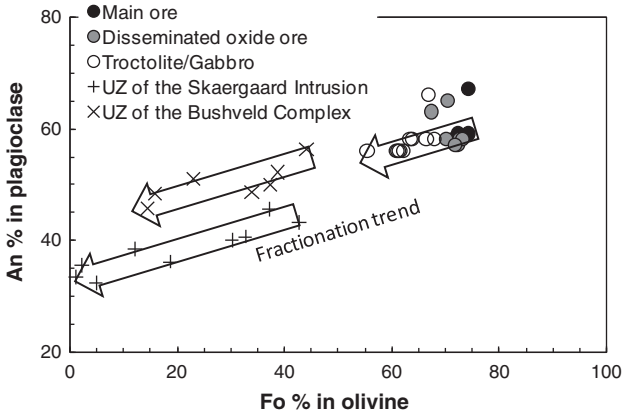

Fig. 6. Binary plots between An content of plagioclase versus Fo content of olivine of the Baima intrusion. The Skaergaard intrusion and the Bushveld Complex data are plotted for reference (data are from McBirney, 1989; Tegner et al., 2006).

6.2.2. Fractional crystallization in shallow magma chamber

The Baima intrusive rocks, including the main ore in LZa in which plagioclase barely occurs, show obvious Sr, Ba and Eu positive anomalies (Pang et al., 2010; Zhou et al., 2008) indicating that rarely plagioclase fractional crystallization had occurred during early differentiation in deep level. Thus, the intrusion of parental magma into the Baima intrusion at a shallow depth probably occurred before abundant plagioclase had crystallized. Hence, we assume that the residual melt after nearly 61% fractionation (chromite + Ol + Opx + Cpx) at 5 kbar which contain 17.55 wt.% FeO_T and 4.93 wt.% TiO_2 at 1185 °C as the parental magma of the Baima intrusion (Table 5).

Field relationships suggest that the layered intrusions in the Panxi area are emplaced at shallow depth, e.g. the Hongge and Xinjie layered intrusions are in contact with Emeishan flood basalts. Considering the similarity in tectonic settings, we therefore assume that the pressure at the time of emplacement of the Baima intrusion was no more than 1.5 kbar.

Toplis and Carroll (1996) suggested that plutonic magmas (e.g. Skaergaard and Kiglapait intrusions) evolved under conditions closed

Table 5
MELTS model results, under 5 kbar and 1.5 kbar.

Primary composition			SiO_2	TiO_2	Al_2O_3	Fe_2O_3	Cr_2O_3	FeO	MnO	MgO	CaO	Na_2O	K_2O	P_2O_5		Fo	
Melt inclusion[a]			46.38	2.25	7.91	1.23	0.20	11.06	0.07	19.68	9.25	1.41	0.40	0.18		91.71	
Under 5 kbar	T	△FMQ[c]	SiO_2	TiO_2	Al_2O_3	Fe_2O_3	Cr_2O_3	FeO	MnO	MgO	CaO	Na_2O	K_2O	P_2O_5	H_2O	$Fo/Mg^{\#}/An$[d]	Density
Crystallized phase[b]	(°C)		wt.%	wt.%	wt.%	wt.%	wt.%	wt.%	wt.%	wt.%	wt.%	wt.%	wt.%	wt.%	wt.%		(g/cm^3)
Olivine	1481	−0.33	41.08					8.42	0.07	50.15	0.28					Fo = 91	3.15
	1315	0.21	40.14					13.31	0.11	46.00	0.44					Fo = 86	3.23
Cr-rich ulvospinel	1415	−0.07		1.87	14.06	8.26	48.45	11.38		15.99						Xchm = 60	4.27
	1185	0.56		17.14	17.45	12.31	8.50	34.30		10.31						Xchm = 11	4.32
Orthopyroxene	1362	0.12	56.47	0.09	1.56	0.45		7.11		32.82	1.48	0.02				$Mg^{\#} = 89$	3.17
	1286	0.28	55.63	0.10	1.79	0.50		8.83		30.30	2.82	0.03				$Mg^{\#} = 86$	3.20
Clinopyroxene	1285	0.28	53.11	0.30	3.07	0.90		6.64		20.84	14.95	0.18				$Mg^{\#} = 83$	3.20
	1185	0.56	47.42	2.33	7.89	1.50		8.09		14.31	17.99	0.47				$Mg^{\#} = 73$	3.30
Residual liquid																	
Ol appear	1481	−0.33	46.37	2.25	7.91	1.23	0.20	11.06	0.07	19.67	9.25	1.41	0.40	0.18			2.82
Cr-rich Usp appear	1415	−0.07	46.98	2.50	8.79	1.37	0.22	11.27	0.07	16.34	10.25	1.57	0.45	0.20			2.82
Opx appear	1362	0.12	47.52	2.70	9.45	1.46	0.17	11.30	0.07	13.93	11.02	1.69	0.48	0.22			2.82
Cpx appear	1285	0.28	46.18	3.16	10.83	1.61	0.10	11.91	0.08	10.86	12.45	1.99	0.57	0.26			2.84
Before Plag appear	1185	0.56	42.77	4.93	15.36	1.86	0.01	15.88	0.15	5.61	8.60	3.35	1.02	0.46			2.90
Under 1.5 kbar	1164	0.26		18.73	13.19	12.30	11.07	33.19		11.53						Xusp = 46	4.32
Cr-rich Tmt	1144	0.41		29.38	5.70	10.59	0.04	44.89		9.40						Xusp = 75	4.41
Plagioclase	1149	0.29	51.19		31.22						13.81	3.59	0.19			An = 68	2.65
	1100	−1.14	53.38		29.69						12.04	4.46	0.43			An = 60	2.64
	1071	−1.98	54.80		28.69						10.88	4.99	0.64			An = 55	2.63
Olivine	1145	0.29	37.78					25.69	0.32	35.76	0.44					Fo = 71	3.43
	1106	−0.91	35.53					37.14	0.78	25.95	0.60					Fo = 55	3.61
	1100	−1.14	35.09					39.35	0.88	24.05	0.63					Fo = 52	3.65
Titanomagnetite	1143	0.31		28.96	6.91	10.31	0.14	43.51		10.18						Xusp = 73	4.37
	1100	−1.14		29.00	4.35	10.73	0.00	50.67		5.26						Xusp = 77	4.57
Clinopyroxene	1129	0.05	34.31	11.51	15.33	1.82		5.51		8.78	22.43	0.31				$Mg^{\#} = 74$	3.44
	1100	−1.14	47.51	2.22	6.32	1.44		9.51		11.72	20.92	0.34				$Mg^{\#} = 69$	3.32
Apatite	977	−3.49									55.82			42.39	1.79		3.06
Residual liquid[b]																	
Cr-rich Tmt appear	1164	0.26	42.75	4.93	15.55	1.86	0.01	15.87	0.15	5.61	8.60	3.35	1.02	0.10	0.20		2.83
Plag appear	1149	0.29	42.86	4.87	15.57	1.84	0.00	15.81	0.15	5.60	8.62	3.36	1.02	0.10	0.20		2.83
Ol appear	1145	0.29	42.79	4.93	15.32	1.86	0.00	16.04	0.15	5.66	8.55	3.36	1.04	0.10	0.20		2.84
Tmt appear	1143	0.31	42.76	4.98	15.19	1.88	0.00	16.17	0.15	5.60	8.53	3.38	1.06	0.10	0.21		2.84
Cpx appear	1129	0.05	44.18	4.47	14.26	1.73	0.00	16.27	0.17	4.94	8.67	3.65	1.27	0.13	0.26		2.82
	1100	−1.14	48.89	2.36	14.22	1.02	0.00	15.98	0.24	2.72	7.00	4.95	1.99	0.21	0.42		2.72
Apa appear	977	−3.49	57.31	0.52	11.29	0.30	0.00	11.66	0.18	0.03	4.74	8.36	3.99	0.54	1.08		2.52

[a] Melt inclusion composition in olivine phenocryst from high-Ti picritic basalt, analyzed by Kamenetsky et al. (2012), represents the initial composition of the Baima intrusion.
[b] Ol = olivine; Usp = ulvospinel; Opx = orthopyroxene; Cpx = clinopyroxene; Plag = plagioclase; Tmt = titanomagnetite; Apa = apatite.
[c] FMQ = fayalite–magnetite–quartz buffer.
[d] Abbreviations same as Tables 1 and 2. $Mg^{\#} = 100[Mg/(Mg+Fe)]$.

to oxygen, because sufficient exchange between the magma and the environment in a large magma chamber is difficult. This means during crystallization of ferrous iron-consuming minerals, the Fe^{3+}/Fe^{2+} ratio and fO_2 of the residual magma will increase before the appearance of Fe–Ti oxide (Snyder et al., 1993; Toplis and Carroll, 1996). As shown in Fig. 5, in LZa and LZb, the Fe^{3+}/Fe^{2+} ratio always decreases from the lower magnetite layer to the upper troctolite. This indicates that the Fe–Ti oxides form and accumulate relatively early in each Fe–Ti-rich parental magma pulse, and responsible to a decreasing fO_2 in residual liquid. Thus, compared with the open to oxygen system, which will keep oxygen fugacity at a constant condition, we prefer to assume that the shallow Baima magma chamber still evolved at a system closed to oxygen.

Jugo (2009) demonstrated that the average fO_2 condition for tholeiitic basalt (e.g. MORB) is FMQ−1 to FMQ+0.5. In natural and experimental silicate melts, sulfur speciation changes from sulfide to sulfate in the fO_2 range of FMQ < fO_2 < FMQ+2 (Jugo et al., 2005; Wallace and Carmichael, 1994). In the Baima intrusion, sulfide minerals, such as pyrrhotite and pentlandite, are common, but no sulfate minerals have been found. It implies that fO_2 of the Baima magma chamber was at least, less than FMQ+0.5. The fO_2 decreases with decreasing pressure, thus, if the residual magma from the shallower magma chamber did not react with wall-rock, the oxygen fugacity would drop down to FMQ+0.26 when it ascent to the Baima intrusion (~1.5 kbar) according to MELTS calculation. At this condition, sulfate species can be negligible in the silicate melt.

Because of the sporadic occurrence of thin brown hornblende reaction rims in the Baima rocks, we assumed that the parental magma absorbed ~0.2 wt.% H_2O from the crust during its ascent to form the Baima intrusion. With this precondition, water content in residual magma might reach to 1.08 wt.% when apatite appears. One problem that we encountered during the MELTS modeling was that apatite starts to crystallize at a relatively early stage, while it commonly occurs at the upper zone of the Baima intrusion, indicating that it is a late-stage phase. In order to compensate for this, P_2O_5 was reduced from 0.46 to 0.1 wt.% in the parental magma according to Shellnutt and Jahn (2010) and Toplis et al. (1994). The assumed parental magma composition and the MELTS simulation result are listed in Table 5 and shown in Fig. 8.

According to the MELTS model, minor Cr-rich magnetite occurred as an early crystallization phase. Hence it is easily enclosed by late crystallized olivine and plagioclase (Fig. 4a, g). Such phenomena also have been found in the Panzhihua and Hongge intrusions (Pang et al., 2008b), in which the high-Cr magnetites occur as inclusions in olivine grains. These inclusions have been used as a condensed evidence for early saturation of Fe–Ti oxides in ferrobasaltic magma (Pang et al., 2008a).

As shown in Fig. 8d, after crystallization fractionation of 0.5% chromite, 3.0% plagioclase, 0.5% olivine, the fO_2 reaches a maximum (FMQ+0.31) well before the appearance of titanomagnetite. The results shown in Table 5 and Fig. 8 illustrate that each crystallization phase

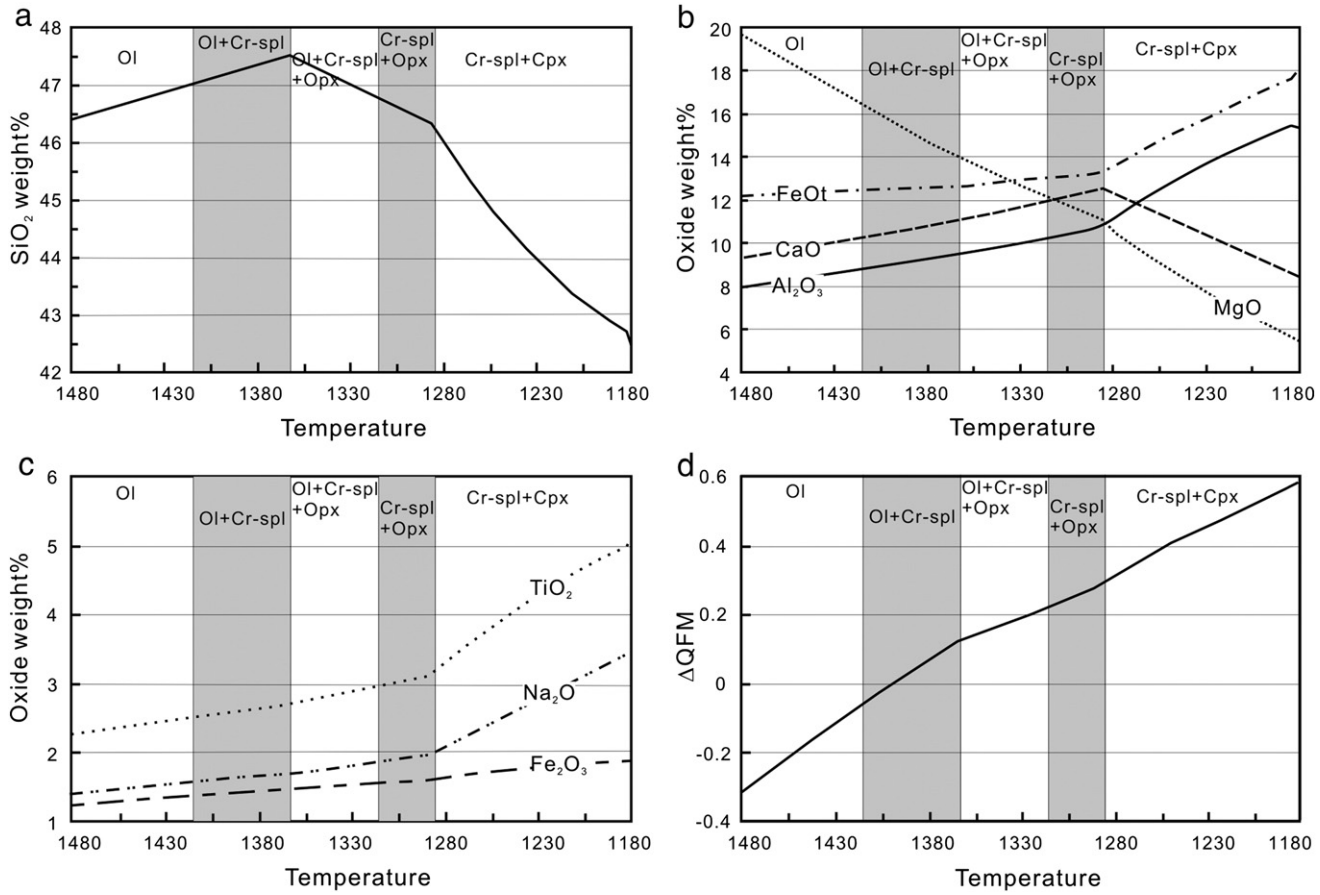

Fig. 7. Results of MELTS modeling using a starting composition of high-Ti picritic melt inclusion in olivine, and assuming a total pressure of 5000 bars, starting temperature of 1480 °C, ending temperature of 1180 °C, under a dry and closed oxygen system.

is controlled by multiply saturated cotectics, and the crystallization order is consistent with the actual cumulate sequence which is observed in the Baima intrusion as described above (Fig. 4).

The modeled compositions of olivine (Fo_{71}) and plagioclase (An_{67}) are well-matched with those measured by electron microprobe (Fo_{74}, An_{68}). A slight difference of Fo content between microprobe data and model results ought to be attributed to the mineral re-equilibration, as the olivine Fo content is sensitive to the variation of Fe^{3+}/Fe^{2+} ratio of the magma (Fig. 5). Furthermore, compared with the mantle-derived olivine, in which CaO content is considered less than 0.1 wt.% (Thompson and Gibson, 2000), the low CaO content (0.02%–0.08%) of olivine in the Baima intrusion (Table 2) illustrates no significant CaO-rich wall rock contamination (Wenzel et al., 2002). These facts demonstrate that wall-rock contamination probably plays a weak role in evaluating oxygen fugacity in The Baima intrusion.

Thus, we draw the conclusion that deep-seated differentiation of mantle-derived picritic basalt under a closed to oxygen system might produce a Fe–Ti-riched residual magma and a relatively high oxygen fugacity condition. These prerequisites are the key factors for early saturation of Fe–Ti oxides in a shallow magma chamber.

7. Emplacement mechanism and thick ore formation

One notable feature of the layered intrusions in the Panxi area is the presence of thick layers of Fe–Ti oxide ore in the lower portions of the intrusive bodies. This geologic characteristic not only needs abundant Fe–Ti oxides to crystallize as an early phase, but also requires them to be concentrated at the lower part of the magma chamber by a series of active dynamic processes.

Reversal of plagioclase An content in cumulate sequence is an evidence of magma replenishment (Pang et al., 2009; Tegner et al., 2006). Three reversals of plagioclase An content in LZa combined with the parallel reversals of whole-rock Cr content demonstrate at least three batches of relatively primary magma replenishment along the lower part of the Baima magma chamber (Fig. 5).

If there is a density difference between the crystal and the liquid, then the crystals must tend to either sink or float in the liquids (Irvine, 1980). In order to further constrain the mechanism that whether the layers were formed by gravitational settling and sorting (Wager and Brown, 1968) or in situ crystallization (Cawthorn and McCarthy, 1980, 1981), the density of different phases needs to be considered. Snyder et al. (1993) found that at all possible oxygen fugacity, the initial fractionation of olivine and plagioclase may cause an increase in liquid density. The density of the residual magma continues to increase until the precipitation of Fe–Ti oxide, after which it begins to drop. This is also confirmed by the MELTS model (Table 5).

There might be relatively little tendency for the plagioclase to crystallize in situ, because the evolved dense iron-rich parental magna currents might be injected along the floor of the magma chamber, as modeled by Irvine (1980) on the Skaergaard intrusion. The lighter crystal mush can probably be retained at the floor by the compaction of surrounding magma. However, crystal mush may also be squeezed from the cumulus, and back to the higher levels by return currents or by the new pulse of hot denser magma (Campbell and Turner, 1989; Huppert and Turner, 1981; Irvine, 1980). The flow orientation was recorded by the elongate shape of plagioclase. The Fe–Ti oxide, once crystallized, might quickly settle

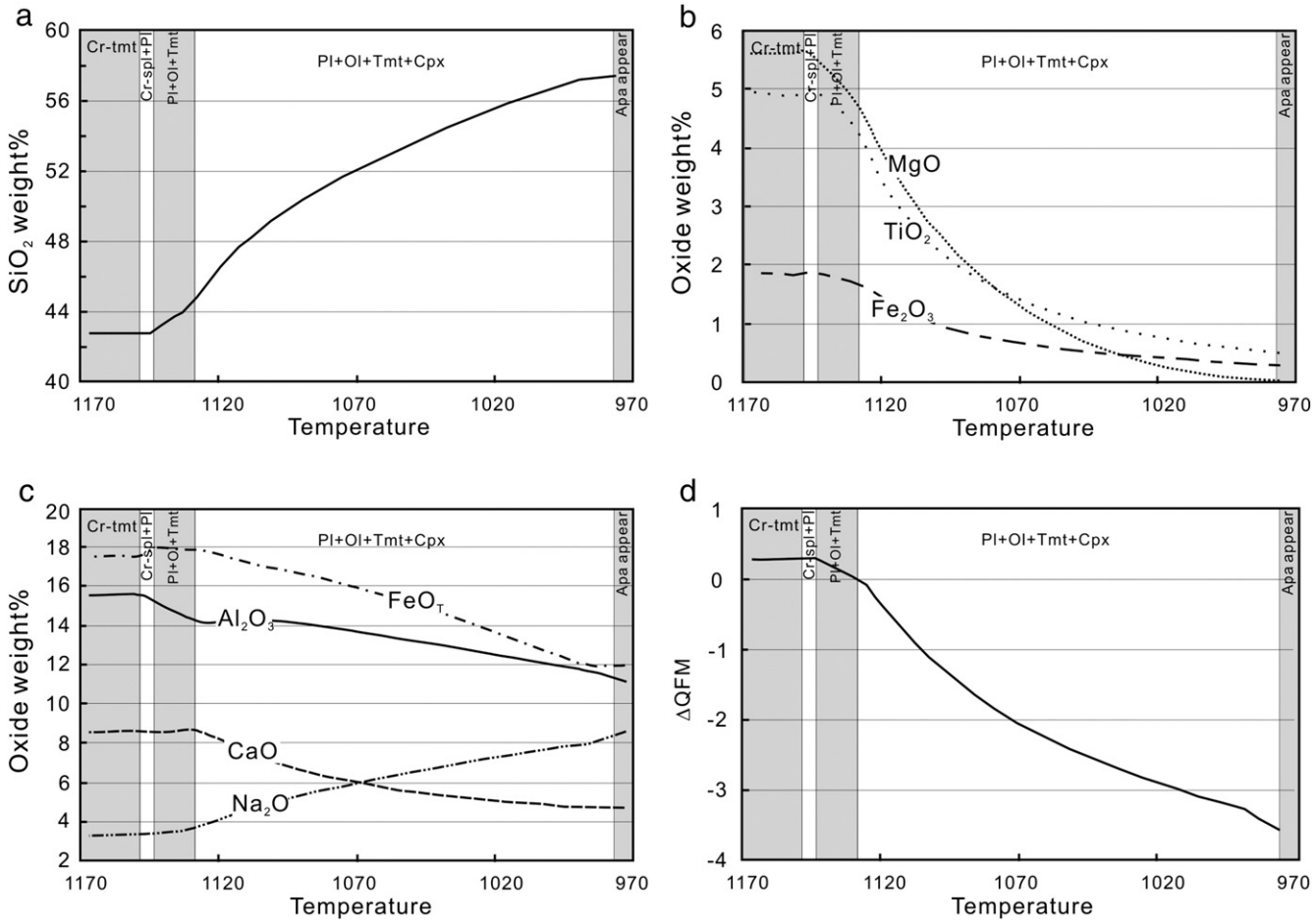

Fig. 8. Oxide content and fO_2 variation with temperature and the crystallization sequence of silicate mineral at 1500 bar. Closed to oxygen system and $H_2O = 0.2$ wt.%.

down to the floor, due to the high density contrast between Fe–Ti oxide and residual magma.

The lithologic and compositional features of the LZa and the LZb indicate that the former was formed by more frequent replenishment of pulses of less evolved magma, which contain higher Cr. Thus, the disseminated oxide layers in the LZa are thicker and contain higher Cr than those in the LZb. The gravitational settling and sorting between the denser Fe–Ti oxides and the lighter plagioclase could be quite sufficient after turbulence by the frequent recharges. In contrast, the disseminated oxide layers in the LZb contain more interlayers of troctolite and are characterized by remarkable rhythmic layers. The double-diffusive convection model proposed by Naslund and McBirney (1996) may be the reasonable explanation for the rhythmic layers in the LZb.

8. Conclusions

The formation of the Fe–Ti oxide ores in the Baima intrusion includes two stages. In the first stage, fractional crystallization of chromite, olivine, orthopyroxene and clinopyroxene from a high-Ti picritic magma produced Fe–Ti-rich magma at a deep level under a closed oxygen system. When such Fe–Ti-rich magma entered the Baima intrusion at a shallower level, magnetite became one of the early liquidus phase cumulates at the base of the intrusion. The formation of the thick Fe–Ti oxide ore layers are closely related to the repeated replenishment of such Fe–Ti-rich magma and the gravitational settling and sorting of the early crystallized Fe–Ti oxides. Wall-rock contamination probably plays a weak role.

Acknowledgment

We thank Zhou Guofu and Liu Shirong for the microprobe analysis. We acknowledge Vadim Kamenetsky for sharing unpublished melt inclusion data. We also appreciated Paul Asimow, Paula Antoshechkin, Mark Ghiorso and Chusi Li for patient guidance and discussions about MELTS software. The comment from A.J. Naldrett has improved an earlier version of the manuscript. This work was funded by the National Basic Research Program of China (2012CB416804), research fund of State Key Laboratory of Ore Deposit Geochemistry (SKLOG-ZY125-06) and NSFC research grants (40730420, 41172090) to Xie-Yan Song.

References

Bai, Z.J., Zhong, H., Naldrett, A.J., Zhu, W.G., Xu, G.W., 2012. Whole-rock and mineral composition constraints on the genesis of the giant Hongge Fe–Ti–V oxide deposit in the Emeishan Large Igneous Province, Southwest China. Econ. Geol. 107, 507–524.

Byers, C.D., Christie, D.M., Muenow, D.W., Sinton, J.M., 1984. Volatile contents and ferric–ferrous ratios of basalt, ferrobasalt, andesite and rhyodacite glasses from the Galapagos 95.5°W propagating rift. Geochim. Cosmochim. Acta 48, 2239–2245.

Campbell, I.H., Turner, J.S., 1989. Fountains in magma chambers. J. Petrol. 30, 885–923.

Carmichael, I.S.E., 1967. The iron–titanium oxides of salic volcanic rocks and their associated ferromagnesian silicates. Contrib. Mineral. Petrol. 14, 36–64.

Cawthorn, R.G., 1996. Layered Intrusions [M]. Elsevier Science, Amsterdam.

Cawthorn, R.G., Ashwal, L.D., 2009. Origin of anorthosite and magnetitite layers in the Bushveld Complex, constrained by major element compositions of plagioclase. J. Petrol. 50, 1607–1637.

Cawthorn, R.G., McCarthy, T.S., 1980. Variations in Cr content of magnetite from the upper zone of the Bushveld Complex — evidence for heterogeneity and convection currents in magma chambers. Earth Planet. Sci. Lett. 46, 335–343.

Cawthorn, R.G., McCarthy, T.S., 1981. Bottom crystallization and diffusion control in layered complexes: evidence from Cr distribution in magnetite from the Bushveld Complex. Trans. Geol. Soc. SA 84, 41–50.

Chen, J., Yang, X., Xiao, L., He, Q., 2010. Coupling of basaltic magma evolution and lithospheric seismic structure in the Emeishan Large Igneous Province: MELTs modeling constraints. Lithos 119, 61–74.
Christie, D.M., Carmichael, I.S.E., Langmuir, C.H., 1986. Oxidation states of mid-ocean ridge basalt glasses. Earth. Planet. Sci. Lett. 79, 397–411.
Chung, S.L., Jahn, B., 1995. Plume–lithosphere interaction in generation of the Emeishan flood basalts at the Permian–Triassic boundary. Geology 23, 889–892.
Eales, H.V., Cawthorn, R.G., 1996. The Bushveld Complex. In: Cawthorn (Ed.), Layered Intrusion [M]. Elsevier Science, Amsterdam, pp. 181–229.
Ghiorso, M.S., Sack, R.O., 1995. Chemical mass transfer in magmatic processes IV. A revised and internally consistent thermodynamic model for the interpolation and extrapolation of liquid–solid equilibria in magmatic systems at elevated temperatures and pressures. Contrib. Mineral. Petr. 119, 197–212.
Harney, D.M.W., Merkle, R.K.W., Von Gruenewaldt, G., 1990. Platinum-group element behavior in the lower part of the upper zone, eastern Bushveld Complex; implications for the formation of the main magnetite layer. Econ. Geology 85, 1777–1789.
He, B., Xu, Y.G., Chung, S.L., Xiao, L., Wang, Y., 2003. Sedimentary evidence for a rapid, kilometer-scale crustal doming prior to the eruption of the Emeishan flood basalts. Earth Planet. Sci. Lett. 213, 391–405.
He, B., Xu, Y.G., Huang, X.L., Luo, Z.Y., Shi, Y.R., Yang, Q.J., Yu, S.Y., 2007. Age and duration of the Emeishan flood volcanism, SW China: geochemistry and SHRIMP zircon U–Pb dating of silicic ignimbrites, post-volcanic Xuanwei Formation and clay tuff at the Chaotian section. Earth Planet. Sci. Lett. 255, 306–323.
He, Q., Xiao, L., Balta, B., Gao, R., Chen, J., 2010. Variety and complexity of the Late-Permian Emeishan basalts: reappraisal of plume–lithosphere interaction processes. Lithos 119, 91–107.
Humphreys, M., 2011. Silicate liquid immiscibility within the crystal mush: evidence from Ti in plagioclase from the Skaergaard intrusion. J. Petrol. 52, 147–174.
Huppert, H.E., Turner, J.S., 1981. A laboratory model of a replenished magma chamber. Earth Planet. Sci. Lett. 54, 144–152.
Irvine, T.N., 1980. Magmatic density currents and cumulus process. Am. J. Sci. 280, 1–58.
Jugo, P.J., 2009. Sulfur content at sulfide saturation in oxidized magmas. Geology 37, 415–418.
Jugo, P.J., Luth, R.W., Richards, J.P., 2005. Experimental data on the speciation of sulfur as a function of oxygen fugacity in basaltic melts. Geochim. Cosmochim. Acta 69, 497–503.
Kamenetsky, V.S., Crawford, A.J., Meffre, S., 2001. Factors controlling chemistry of magmatic spinel: an empirical study of associated olivine, Cr-spinel and melt inclusions from primitive rocks. J. Petrol. 42, 655–671.
Kamenetsky, V.S., Chung, S.L., Kamenetsky, M.B., Kuzmin, D.V., 2012. Picrites from the Emeishan Large Igneous Province, SW China: a compositional continuum in primitive magmas and their respective mantle sources. J. Petrol. 53 (10), 2095–2113.
Klemme, S., Gunther, D., Hametner, K., Prowatke, S., Zack, T., 2006. The partitioning of trace elements between ilmenite, ulvospinel, armalcolite and silicate melts with implications for the early differentiation of the moon. Chem. Geol. 234, 251–263.
Lattard, D., Partzsch, G.M., 2001. Magmatic crystallization experiments at 1 bar in systems closed to oxygen: a new/old experimental approach. Eur. J. Mineral. 13, 467–478.
Leeman, W.P., Ma, M.S., Murali, A.V., Schmitt, R.A., 1978. Empirical estimation of the magnetite/liquid distribution coefficients for some transition elements. Contrib. Mineral. Petrol. 65, 269–272.
Ma, Y., Ji, X.T., Li, J.C., Huang, M., Kan, Z.Z., 2003. Mineral Resources of the Panzhihua Region. Sichuan Science and Technology Press, Chengdu . (275 pp. (in Chinese)).
McBirney, A., 1989. The Skaergaard layered series: I. structure and average compositions. J. Petrol. 30, 363–397.
McBirney, A.R., 1996. The Skaergaard intrusion. In: Cawthorn (Ed.), Layered Intrusion [M]. Elsevier Science, Amsterdam, pp. 147–180.
Nakamura, Y., Fujimaki, H., 1986. Hf, Zr, and REE partition coefficients between ilmenite and liquid: implications for lunar petrogenesis. J. Geophys. Res. 91, 239–250.
Naslund, H.R., 1983. The effect of oxygen fugacity on liquid immiscibility in iron-bearing silicate melts. Am. J. Sci. 283, 1034–1059.
Naslund, H.R., McBirney, A.R., 1996. Mechanisms of formation of igneous layering. In: Cawthorn (Ed.), Layered Intrusion [M]. Elsevier Science, Amsterdam, pp. 1–43.
Pang, K.N., Zhou, M.F., Lindsley, D., Zhao, D.G., Malpas, J., 2008a. Origin of Fe–Ti oxide ores in mafic intrusions: evidence from the Panzhihua intrusion, SW China. J. Petrol. 49, 295–313.
Pang, K.N., Li, C.S., Zhou, M.F., Ripley, E.M., 2008b. Abundant Fe–Ti oxide inclusions in olivine from the Panzhihua and Hongge layered intrusions, SW China: evidence for early saturation of Fe–Ti oxides in ferrobasaltic magma. Contrib. Mineral. Petr. 156, 307–321.
Pang, K.N., Li, C.S., Zhou, M.F., Ripley, E.M., 2009. Mineral compositional constraints on petrogenesis and oxide ore genesis of the late Permian Panzhihua layered gabbroic intrusion, SW China. Lithos 110, 199–214.
Pang, K.N., Zhou, M.F., Qi, L., Shellnutt, G., Wang, C.Y., Zhao, D.G., 2010. Flood basalt-related Fe–Ti oxide deposits in the Emeishan Large Igneous Province, SW China. Lithos 119, 123–136.
Panxi Geological Unit, 1984. Mineralization and Exploration Forecasting of V–Ti Magnetite Deposits in the Panzhihua–Xichang Region. (in Chinese).
Philpotts, A.R., 1982. Composition of immiscible liquids in volcanic rocks. Contrib Mineral Petrol. 80, 201–218.
Qi, L., Zhou, M.F., 2008. Platinum-group elemental and Sr–Nd–Os isotopic geochemistry of Permian Emeishan flood basalts in Guizhou Province, SW China. Chem. Geol. 248, 83–103.
Qi, L., Hu, J., Gregoire, D.C., 2000. Determination of trace elements in granites by inductively coupled plasma mass spectrometry. Talanta 51, 507–513.
Reynolds, I.M., 1985. The nature and origin of titaniferous magnetite-rich layered in the upper zone of the Bushveld Complex: a review and synthesis. Econ. Geol. 80, 1089–1108.
Rhodes, J., Vollinger, M., 2005. Ferric/ferrous ratios in 1984 Mauna Loa lavas: a contribution to understanding the oxidation state of Hawaiian magmas. Contrib. Mineral. Petrol. 149, 666–674.
Scoon, R.N., Eales, H.V., 2002. Unusual Fe–Ti–Cr spinel from discordant bodies of iron-rich ultramafic pegmatite at the Amandelbult Platinum mine, northwestern Bushveld Complex. Mineral. Mag. 66, 857–879.
Shellnutt, J.G., Jahn, B.M., 2010. Formation of the Late Permian Panzhihua plutonic–hypabyssal–volcanic igneous complex: implications for the genesis of Fe–Ti oxide deposits and A-type granites of SW China. Earth. Planet. Sci. Lett. 289, 509–519.
Snyder, D., Carmichael, I.S.E., Wiebe, R.A., 1993. Experimental study of liquid evolution in an Fe-rich, layered mafic intrusion: constraints of Fe–Ti oxide precipitation on the T–fO_2 and T–ρ paths of tholeiitic magmas. Contrib. Mineral. Petrol. 113, 73–86.
Song, X.Y., Zhou, M.F., Hou, Z.Q., Cao, Z.M., Wang, Y.L., Li, Y.G., 2001. Geochemical constraints on the mantle source of the upper Permian Emeishan continental flood basalts, southwestern China. Int. Geol. Rev. 43, 213–225.
Song, X.Y., Zhou, M.F., Cao, Z.M., Robinson, P.T., 2004. Late Permian rifting of the South China Craton caused by the Emeishan mantle plume? J. Geol. Soc. Lond. 161, 773–781.
Song, X.Y., Zhang, C.J., Hu, R.Z., Zhong, H., Zhou, M.F., Ma, R.Z., Li, Y.G., 2005. Genetic links of magmatic deposits in the Emeishan Large Igneous Province with dynamics of mantle plume. J. Mineralog. Petrol. 25, 35–44 (in Chinese).
Song, X.Y., Zhou, M.F., Tao, Y., Xiao, J.F., 2008. Controls on the metal compositions of magmatic sulfide deposits in the Emeishan Large Igneous Province, SW China. Chem. Geol. 253, 38–49.
Song, X.Y., Keays, R.R., Xiao, L., Qi, H.W., Ihlenfeld, C., 2009. Platinum-group element geochemistry of the continental flood basalts in the central Emeishan Large Igneous Province, SW China. Chem. Geol. 262, 246–261.
Tegner, C., Cawthorn, R.G., Kruger, F.J., 2006. Cyclicity in the main and upper zones of the Bushveld Complex, South Africa: crystallization from a zoned magma sheet. J. Petrol 47, 2257–2279.
Thompson, R., Gibson, S., 2000. Transient high temperatures in mantle plume heads inferred from magnesian olivines in Phanerozoic picrites. Nature 407, 502–506.
Toplis, M.J., Carroll, M.R., 1995. An experimental-study of the influence of oxygen fugacity on Fe–Ti oxide stability, phase-relations, and mineral-melt equilibria in ferro-basaltic systems. J. Petrol. 36, 1137–1170.
Toplis, M.J., Carroll, M.R., 1996. Differentiation of ferro-basaltic magmas under conditions open and closed to oxygen: implications for the Skaergaard intrusion and other natural systems. J. Petrol. 37, 837–858.
Toplis, M., Dingwell, D., Libourel, G., 1994. The effect of phosphorus on the iron redox ratio, viscosity, and density of an evolved ferro-basalt. Contrib. Mineral. Petr. 117, 293–304.
VanTongeren, J., Mathez, E., 2012. Large-scale liquid immiscibility at the top of the Bushveld Complex. Geology 40, 491–494.
Wager, L.R., Brown, G.M., 1968. Layered Igneous Rocks [M]. Oliver and Boyd, Edinburgh and London.
Wallace, P.J., Carmichael, I.S.E., 1994. S speciation in submarine basaltic glasses as determined by measurements of SKÁ X-ray wavelength shifts. Am. Mineral. 79, 161–167.
Wenzel, T., Baumgartner, L.P., Brugmann, G.E., Konnikov, E.G., Kislov, E.V., 2002. Partial melting and assimilation of dolomitic xenoliths by mafic magma: the Ioko-Dovyren intrusion (north Baikal region, Russia). J. Petrol. 43, 2049–2074.
Williams, H.M., McCammon, C.A., Peslier, A.H., Halliday, A.N., Teutsch, N., Levasseur, S., Burg, J.P., 2004. Iron isotope fractionation and the oxygen fugacity of the mantle. Science 304, 1656–1659.
Wood, B.J., Bryndzia, L.T., Johnson, K.E., 1990. Mantle oxidation state and its relationship to tectonic environment and fluid speciation. Science 248, 337–345.
Xiao, L., Xu, Y.G., Mei, H.J., Zheng, Y.F., He, B., Pirajno, F., 2004. Distinct mantle sources of low-Ti and high-Ti basalts from the western Emeishan Large Igneous Province, SW China: implications for plume–lithosphere interaction. Earth. Planet. Sci. Lett. 228, 525–546.
Xu, Y.G., Chung, S.L., Jahn, B.M., Wu, G.Y., 2001. Petrologic and geochemical constraints on the petrogenesis of Permian–Triassic Emeishan flood basalts in southwestern China. Lithos 58, 145–168.
Zhong, H., Zhu, W.G., 2006. Geochronology of layered mafic intrusions from the Pan-Xi area in the Emeishan Large Igneous Province, SW China. Miner. Deposit. 41, 599–606.
Zhong, H., Campbell, I.H., Zhu, W.G., Allen, C.M., Hu, R.Z., Xie, L.W., He, D.F., 2011. Timing and source constraints on the relationship between mafic and felsic intrusions in the Emeishan Large Igneous Province. Geochim. Cosmochim. Ac. 75, 1374–1395.
Zhou, M.F., Malpas, J., Song, X.Y., Robinson, P.T., Sun, M., Kennedy, A.K., Lesher, C.M., Keays, R.R., 2002. A temporal link between the Emeishan Large Igneous Province (SW China) and the end-Guadalupian mass extinction. Earth. Planet. Sci. Lett. 196, 113–122.
Zhou, M.F., Robinson, P.T., Lesher, C.M., Keays, R.R., Zhang, C.J., Malpas, J., 2005. Geochemistry, petrogenesis and metallogenesis of the Panzhihua gabbroic layered intrusion and associated Fe–Ti–V oxide deposits, Sichuan Province, SW China. J. Petrol. 46, 2253–2280.
Zhou, M.F., Arndt, N.T., Malpas, J., Wang, C.Y., Kennedy, A.K., 2008. Two magma series and associated ore deposit types in the Permian Emeishan Large Igneous Province, SW China. Lithos 103, 352–368.